

Furin Cleavage Site Is Key to SARS-CoV-2 Pathogenesis

Bryan A. Johnson^{1*}, Xuping Xie^{2*}, Birte Kalveram³, Kumari G. Lokugamage¹, Antonio Muruato¹, Jing Zou², Xianwen Zhang², Terry Juelich³, Jennifer K. Smith³, Lihong Zhang³, Nathen Bopp³, Craig Schindewolf¹, Michelle Vu¹, Abigail Vanderheiden^{5,6,7}, Daniele Swetnam², Jessica A. Plante¹, Patricia Aguilar³, Kenneth S. Plante¹, Benhur Lee⁸, Scott C. Weaver^{1,4}, Mehul S. Suthar^{5,6,7}, Andrew L. Routh², Ping Ren³, Zhiqiang Ku⁹, Zhiqiang An⁹, Kari Debbink¹⁰, Pei Yong Shi^{2,4,#}, Alexander N. Freiberg^{3,4,#}, Vineet D. Menachery^{1,4,#}

¹Departments of Microbiology and Immunology, ²Biochemistry and Molecular Biology,

³Pathology, ⁴Institute for Human Infection and Immunity, University of Texas Medical Branch, Galveston, TX, USA

⁵ Department of Pediatrics, ⁶Emory Vaccine Center, Emory University School of Medicine, Atlanta, GA, USA.

⁷Yerkes National Primate Research Center, Atlanta, GA, USA

⁸Icahn School of Medicine at Mount Sinai, New York, NY, USA

⁹Texas Therapeutics Institute, Brown Foundation Institute of Molecular Medicine, University of Texas Health Science Center at Houston, Houston, USA.

¹⁰Bowie State University, Bowie, MD, USA

*Equal contributions

#Co-senior authors

Corresponding Author: Vineet D. Menachery

Address: University of Texas Medical Branch, 301 University Blvd, Route #0610 Galveston, TX 77555

Email: Vimenach@utmb.edu

Article Summary: A deletion of the furin cleavage site in SARS-CoV-2 amplifies replication in Vero cells, but attenuates replication in respiratory cells and pathogenesis *in vivo*. Loss of the furin site also reduces susceptibility to neutralization *in vitro*.

Running title: Furin cleavage site is key to SARS-CoV-2 replication and pathogenesis.

Keywords: Coronavirus, 2019-nCoV, SARS-CoV-2, COVID-19, furin-cleavage, spike

1 **Abstract**

2 SARS-CoV-2 has resulted in a global pandemic and shutdown economies around the world.
3 Sequence analysis indicates that the novel coronavirus (CoV) has an insertion of a furin
4 cleavage site (PRRAR) in its spike protein. Absent in other group 2B CoVs, the insertion may
5 be a key factor in the replication and virulence of SARS-CoV-2. To explore this question, we
6 generated a SARS-CoV-2 mutant lacking the furin cleavage site (Δ PRRA) in the spike protein.
7 This mutant virus replicated with faster kinetics and improved fitness in Vero E6 cells. The
8 mutant virus also had reduced spike protein processing as compared to wild-type SARS-CoV-2.
9 In contrast, the Δ PRRA had reduced replication in Calu3 cells, a human respiratory cell line, and
10 had attenuated disease in a hamster pathogenesis model. Despite the reduced disease, the
11 Δ PRRA mutant offered robust protection from SARS-CoV-2 rechallenge. Importantly, plaque
12 reduction neutralization tests (PRNT₅₀) with COVID-19 patient sera and monoclonal antibodies
13 against the receptor-binding domain found a shift, with the mutant virus resulting in consistently
14 reduced PRNT₅₀ titers. Together, these results demonstrate a critical role for the furin cleavage
15 site insertion in SARS-CoV-2 replication and pathogenesis. In addition, these findings illustrate
16 the importance of this insertion in evaluating neutralization and other downstream SARS-CoV-2
17 assays.

18 **Importance**

19 As COVID-19 has impacted the world, understanding how SARS-CoV-2 replicates and causes
20 virulence offers potential pathways to disrupt its disease. By removing the furin cleavage site,
21 we demonstrate the importance of this insertion to SARS-CoV-2 replication and pathogenesis.
22 In addition, the findings with Vero cells indicate the likelihood of cell culture adaptations in virus
23 stocks that can influence reagent generation and interpretation of a wide range of data including
24 neutralization and drug efficacy. Overall, our work highlights the importance of this key motif in
25 SARS-CoV-2 infection and pathogenesis.

26 **Introduction**

27 The rapid emergence of severe acute respiratory syndrome 2 coronavirus (SARS-CoV-2) at the
28 end of 2019 ushered in a pandemic that has led to over 24 million cases and over 800,000
29 deaths ^{1,2}. The novel coronavirus, like its predecessors severe acute respiratory syndrome
30 coronavirus SARS-CoV and Middle East Respiratory Syndrome (MERS)-CoV induces
31 potentially severe respiratory disease including fever, breathing difficulty, bilateral lung
32 infiltration, and in many cases, death ^{3,4}. While SARS-CoV-2 shares a similar genomic structure
33 and protein homology with SARS-CoV, its ability to spread asymptotically and cause a range
34 of mild to severe disease distinguishes it from the earlier pandemic CoV ⁵. In exploring the
35 differences, attention has been paid to the spike (S) protein, a key glycoprotein responsible for
36 receptor binding and entry into the cell. Following receptor recognition, the S protein is
37 subsequently cleaved at two sites, S1/S2 and the S2' site to facilitate virus entry into a cell.
38 Initial structural work has indicated that SARS-CoV-2 has greater affinity for the ACE2 receptor
39 than the original SARS-CoV ^{6,7}. In addition, changes in the N-terminal domain in addition to the
40 receptor-binding domain indicate potential differences in attachment that may drive changes to
41 transmission or virulence ⁸. However, the majority of attention has focused on a potentially
42 critical insertion of a furin cleavage site upstream of the S1 cleavage site in spike ⁹. Absent in
43 other group 2B CoVs, the four additional amino acids (PRRA) form the classic RXXR motif
44 cleaved by many serine proteases when added to the conserved R found at the SARS-CoV-2
45 S1 cleavage site (PRRAR) ¹⁰. Notably, furin cleavage sites have been observed in other
46 virulent pathogens like HIV, avian influenza strains (H5 and H7) as well as Ebola ¹¹. In fact, furin
47 cleavage sites are found in a number of other CoV family members including MERS-CoV,
48 HKU1-CoV, and OC43-CoV ^{12,13}; given the range of disease associated with these CoV strains,
49 the furin cleavage site does not necessarily predetermine virulence. However, given its
50 absence in other group 2B CoVs and the major differences in disease compared to SARS-CoV,

51 a better understanding of the role of the furin cleavage site during SARS-CoV-2 infection is
52 needed.

53 In this manuscript, we utilized a reverse genetic system to generate a SARS-CoV-2
54 mutant that lacked the furin cleavage site insertion ¹⁴. The mutant, ΔPRRA, had augmented
55 replication and improved fitness in Vero E6 cells relative to wild type (WT) SARS-CoV-2. It also
56 had reduced spike processing as compared to the WT virus. In contrast, the ΔPRRA mutant
57 was attenuated in Calu3 cells, a human respiratory cell line, and had altered S protein
58 processing as compared to Vero cells. *In vivo*, the ΔPRRA mutant had attenuated disease in
59 hamsters despite robust, and sometimes augmented viral replication. Importantly, prior
60 infection with the ΔPRRA mutant protected hamsters from subsequent rechallenge with WT
61 SARS-CoV-2. Finally, neutralization assays that used the ΔPRRA mutant had lower PRNT₅₀
62 values with both COVID-19 patient sera and monoclonal antibodies against the receptor-binding
63 domain (RBD). Together, the results indicate a critical role for the furin cleavage site in SARS-
64 CoV-2 infection and potential complications in interpreting research related to this virus
65 infection.

66

67 **Results**

68 The SARS-CoV-2 spike protein is >75% conserved in amino acid sequence across the group
69 2B CoV family with the majority of the differences occurring in the N-terminal domain and
70 receptor-binding domain in the S1 portion (**S. Fig. 1A**). The insertion of a furin cleavage site
71 (PRRA) upstream of the S1 cleavage site distinguishes SARS-CoV-2 from other group 2B CoV
72 sequences including SARS-CoV and RATG13, the closest bat-derived CoV sequence (**S. Fig.**
73 **1B**). To evaluate the impact of the furin cleavage site insertion, we generated a mutant virus
74 lacking the PRRA motif using our SARS-CoV-2 reverse genetic system (**Fig. 1A**) ¹⁴. Based on
75 the SARS-CoV S protein structure, the insertion occurs in an exterior loop of the SARS-CoV-2
76 spike below the spike globular head and away from the receptor binding domain (**Fig. 1B**) ¹⁵.
77 Using homology modeling based on the SARS-CoV S protein structure, we found the PRRA
78 insertion in an extended loop (cyan). Deletion of PRRA insertion is predicted to shorten the
79 loop, but importantly, not disrupt the overall structure of the spike protein. Following
80 electroporation, we were able to recover the SARS-CoV-2 ΔPRRA mutant with stock virus titer
81 roughly equivalent to the wild-type (WT) virus. Surprisingly, the SARS-CoV-2 ΔPRRA mutant
82 virus produced a larger plaque size on Vero E6 cells than WT virus, suggesting potential
83 changes in viral replication and spread in the absence of the furin cleavage site insertion (**S.**
84 **Fig. 1C**).

85 **Distinct replication kinetics and spike cleavage for the ΔPRRA mutant in Vero E6 cells.**

86 To evaluate viral replication, we infected Vero E6 cells with the WT and ΔPRRA SARS-CoV-2.
87 Previous work has found robust replication of SARS-CoV-2 in Vero E6 cell and these cells are
88 often used for propagation, including for inactivated vaccine production ¹⁶. Following low MOI
89 (0.01 plaque forming units (PFU)/cell) infection, both WT and ΔPRRA SARS-CoV-2 mutant
90 replicated to similar end-point titers (**Fig. 1C**). However, the ΔPRRA had a 25-fold increase in
91 viral titer at 24 hours post infection (HPI) relative to WT. The increased replication was

92 accompanied by more cytopathic effect (CPE) at 24 HPI; by 48 HPI, both mutant and WT levels
93 had nearly 100% CPE. Together, the results suggested the loss of the furin cleavage site
94 augmented replication in Vero E6 cells.

95 We next evaluated spike processing of the Δ PRRA mutant relative to WT SARS-CoV-2
96 as well as the original SARS-CoV. Vero E6 cells were infected at an MOI of ~0.1 for 24 h and
97 purified virions were isolated from supernatants using ultracentrifugation and a sucrose cushion.
98 The pelleted virus was subsequently examined for spike and nucleocapsid (N) protein levels by
99 western blotting. Following SARS-CoV infection, the majority of the spike protein was observed
100 in its full-length form (98.6%) (**Fig. 1D, S. Fig. 2A**), consistent with the absence of processing.
101 In contrast, the WT SARS-CoV-2 virions had a significant reduction in full-length spike protein
102 (40.4%). Instead, the most abundant form of the spike protein was the S1/S2 cleavage product
103 (59.6%). Finally, the Δ PRRA mutant spike protein had mostly full-length spike (85.5%), similar
104 to SARS-CoV, with only minimal processing to the S1/S2 cleavage form (14.5%). Given similar
105 levels of viral N protein, these results illustrate the differences in processing between SARS-
106 CoV and SARS-CoV-2. In addition, the data show that processing of the SARS-CoV-2 spike is
107 driven primarily by the furin cleavage site following infection of Vero E6 cells.

108 Given the replication advantage noted at 24 HPI (**Fig. 1D**), we next evaluated the fitness
109 of the Δ PRRA mutant relative to WT SARS-CoV-2 in a competition assay. Using plaque-
110 forming units to determine the input, we mixed the WT and mutant viruses at different ratios in
111 Vero E6 cells, and used a RT-PCR approach to evaluate their overall fitness after 24 hours (**Fig.**
112 **1E, S. Fig 2B-C**). At a 50:50 input ratio, the Δ PRRA mutant quickly outcompeted WT becoming
113 nearly 90% of the viral population based on both RT-PCR distinguishing the two viruses.
114 Similarly, a 90:10 WT to mutant input ratio resulted in ~65% of the viral sequences
115 corresponding with the mutant virus, illustrating the advantage of the furin site deletion after only
116 24 HPI. The inverse 10:90 WT to mutant input ratio produced <3% of the WT virus and solidified

117 the major advantage of the ΔPRRA mutant in Vero E6 cells. We further confirmed these data
118 using deep sequencing analysis (**S. Fig. 2D**). Together, the results indicate that deletion of the
119 furin cleavage site provides a fitness advantage in Vero E6 cells and a potentially potent cell
120 culture adaptation.

121 **Attenuation of SARS-CoV-2 ΔPRRA in Calu3 respiratory cells.** Having established
122 augmented replication, altered spike processing, and enhanced fitness in Vero E6 cells, we next
123 evaluated the ΔPRRA mutant in a more relevant cell type. Previously, Calu3 2B4 cells, a
124 human lung adenocarcinoma cell line, had been sorted for ACE2 expression and used to study
125 influenza and coronaviruses^{17,18}. In this study, we infected Calu3 2B4 with WT and ΔPRRA
126 SARS-CoV-2 at MOI 0.01. Following infection, we found robust replication of WT SARS-CoV-2
127 peaking 72 HPI. In contrast, the ΔPRRA mutant virus was attenuated relative to WT beginning
128 48 HPI (**Fig. 1F**). At both 48 and 72 HPI, the ΔPRRA mutant had 1-log reduction in viral titer,
129 contrasting the improved replication observed in Vero E6 cells. These data indicate that the loss
130 of the furin cleavage site impairs replication in Calu3 cells and suggests SARS-CoV-2 requires
131 the PRRA motif for efficient replication in these respiratory cells.

132 We subsequently repeated examination of the spike processing on virions from Calu3
133 2B4 cells for the ΔPRRA mutant. Similar to studies with Vero E6 cells, we infected Calu3 2B4
134 cells with SARS-CoV, SARS-CoV-2 WT, and ΔPRRA mutants at MOI 0.1. Given the reduced
135 viral yields in Calu3 2B4 (**Fig. 1F**), we allowed replication to occur until 48 HPI before capturing
136 supernatants and recovering purified virions. Consistent with findings in Vero E6 cells, the
137 western blot of SARS-CoV virions showed the majority of spike protein was retained in the full-
138 length form (**Fig. 1G, S. Fig. 2E**). In contrast, the WT SARS-CoV-2 showed the majority of its
139 spike protein had been cleaved to the S1/S2 form. Comparing to Vero E6 cells, spike
140 processing to the S1/S2 form was more robust in Calu3 showing a ~87.3% at S1/S2 as
141 compared to 59.6% in Vero E6 cells. Surprisingly, the ΔPRRA mutant also showed a significant

142 increase in the S1/S2 cleavage product relative to its Vero spike blots. While the Δ PRRA has
143 reduced overall infection, a clear band was visible at the S1/S2 cleavage site and represents
144 more than 2 times as much S1/S2 cleavage product (33.1% vs 14.5%) compared to Vero E6
145 results. While more full-length spike is observed in the WT virus infection, the Calu3 results
146 indicate that even without the furin cleavage site, there is significant processing of the SARS-
147 CoV-2 spike. The results suggest that while the furin cleavage site is key in SARS-CoV-2 spike
148 processing, other factors outside the PRRA insertion play a role in the efficient cleavage of the
149 SARS-CoV-2 spike in a cell type-dependent manner.

150 ***In vivo* attenuation of Δ PRRA mutant.** Having established contrasting results with *in vitro*
151 studies, we next sought to evaluate the SARS-CoV-2 Δ PRRA mutant in an *in vivo* model. Early
152 attempts found mouse models non-viable for SARS-CoV-2 infection ¹⁹; therefore we shifted to
153 the hamster model which shows modest disease following infection with SARS-CoV-2 infection
154 ²⁰. Four male hamsters were challenged with 10^5 PFU of either WT SARS-CoV-2 or Δ PRRA
155 mutant (**Fig. 2A**). The animals were subsequently monitored for 28 days with periodic measures
156 of their body weight and disease signs. In addition, nasal washes and oral swabs were taken at
157 day 2-7, 14, 21, and 28 days post infection (DPI). Following infection with WT SARS-CoV-2,
158 hamsters steadily lost weight starting at day 2 and continuing through day 8 with peak weight
159 loss nearing 15% (**Fig. 2B, S. Fig. 3A**). These WT-infected hamsters also had disease scores
160 that peaked between days 8 and 10, when animals showed signs including ruffled fur, hunched
161 posture, and reduced activity requiring additional monitoring (**Fig. 2C, S. Fig. 3B**). Despite this
162 severe disease, the WT-infected hamsters subsequently recovered and regained their starting
163 weight by day 15 (**S. Fig. 3A**). In contrast, hamsters infected with SARS-CoV-2 Δ PRRA
164 showed minimal weight loss over the course of infection (**Fig. 3B, S. Fig. 3A**). Over the first
165 four days of infection, the Δ PRRA infected hamsters showed 2-3% weight loss, but remained
166 close to their starting weight through day 10. In addition, the Δ PRRA mutant-infected hamsters

167 had no change in disease score over the course of infection, distinguishing it from symptomatic
168 disease observed following WT SARS-CoV-2 infection. The hamsters in both groups eventually
169 gained a significant amount of weight after day 10 over the remainder of the 28-day time course
170 (**S. Fig. 3A**).

171 Despite attenuated disease, the viral titers revealed augmented replication of the
172 Δ PRRA mutant relative to WT SARS-CoV-2. Examining nasal washes, both WT and Δ PRRA
173 infected hamsters had similar viral titers 2 DPI (**Fig. 2D**). However, augmented Δ PRRA
174 replication was observed at both days 3 and 4 relative to the WT SARS-CoV-2. In addition, the
175 WT virus was cleared from the nasal washes a day earlier than the Δ PRRA mutant, although no
176 plaque forming units were detected after day 7 in either of the hamster groups. Evaluating oral
177 swabs for viral RNA, a similar pattern was observed with augmented viral RNA at days 3 and 4
178 in the Δ PRRA mutant relative to WT (**Fig. 2E**). Notably, the viral RNA in the swabs stayed
179 positive though day 7 with augmented WT viral RNA yield observed at the latest time point
180 relative to Δ PRRA. Together, the results suggest that despite the attenuation in disease, the
181 Δ PRRA mutant is capable of robust replication in the oral and nasal cavity of hamsters following
182 infection.

183 **Infection with Δ PRRA mutant protects from SARS-CoV-2 rechallenge.** We next evaluated if
184 infection with Δ PRRA offered protection from further SARS-CoV-2 infection. Hamsters
185 previously infected with either WT SARS-CoV-2 or the Δ PRRA mutant were rechallenged with
186 10^5 PFU of WT SARS-CoV-2 28 days post initial infection (**Fig. 2F**). The rechallenged hamsters
187 were monitored for disease and weight loss over a 21-day time course. Contrasting initial
188 challenge, both WT and Δ PRRA infected hamsters were protected from weight loss following
189 rechallenge (**Fig. 2G and S. Fig. 3B**). Hamsters infected with WT SARS-CoV-2 initially had no
190 weight loss over the course of infection; however, mild disease (ruffled fur) was observed in a
191 subset of animals (**Fig. 2H**). In contrast, rechallenge of Δ PRRA mutant-infected hamsters

192 produced neither weight loss nor any evidence of disease. Nasal wash titers and viral RNA from
193 oral swabs showed viral replication in both WT- and Δ PRRA-infected animals at day 2 and 3;
194 however, the overall viral loads were significantly reduced compared to initial challenge (**Fig. 2I**
195 & **J**). In addition, plaque forming virus appeared to be cleared around day 4 following
196 rechallenge with low viral RNA loads found in oral swabs at corresponding time points. The
197 results indicate that infection with the Δ PRRA mutant protects hamsters from disease upon
198 rechallenge, but does not provide sterilizing immunity.

199 **Loss of furin cleavage site alters COVID19 serum neutralization.** We next sought to
200 evaluate the impact of the furin cleavage site deletion on virus neutralization by COVID-19
201 patient sera and monoclonal antibodies (mAB) against the SARS-CoV-2 receptor binding
202 domain (RBD). To quantitate neutralization, we generated a Δ PRRA mutant containing the
203 mNeonGreen (mNG) reporter in open reading frame 7 and subsequently compared
204 neutralization results to the WT SARS-CoV-2 mNG reporter assay as previously described²¹
205 (**Fig. 3A**). Examining seventeen COVID-19 human sera samples, we found nearly uniform
206 reduction in PRNT₅₀ values against the Δ PRRA mutant as compared to the WT control virus
207 (**Fig. 3B**). The lower PRNT₅₀ values were observed in sera whether the samples were from low,
208 intermediate, or high neutralizing COVID19 patients (**Fig. 3C-E**) and averaged a 2.3-fold
209 reduction across the 17 human sera. The consistency in the reduction suggested several
210 possibilities: One is that virions themselves are altered in the conformation of the spike on the
211 surface. In this situation, the processing or loss of spikes may permit access to more cryptic
212 sites on the spike S2 or other regions allowing the WT virus to be more easily neutralized by
213 non-receptor binding domain antibodies. A second possibility is that the loss of the furin
214 cleavage site leaves more intact spike molecules on the virion surface requiring more antibodies
215 to neutralize the Δ PRRA mutant than WT SARS-CoV-2. To explore this question, we examined
216 the Δ PRRA mutant neutralization in the presence of three monoclonal antibodies (mAB) that

217 target the SARS-CoV-2 receptor binding domains (RBD) (**Fig. 3F-H**). Each mAB targets a
218 different site in the RBD, but each had similar reduction in the mAB serum neutralization levels
219 between WT and Δ PRRA. The need for more mAB or polyclonal COVID patient sera suggest
220 that Δ PRRA has more spike proteins that must be neutralized. Together, the results highlight
221 significant differences in the neutralization between the WT and Δ PRRA SARS-CoV-2 mutants.

222

223 **Discussion**

224 The loss of the furin cleavage site in the SARS-CoV-2 spike has a major impact on infection and
225 pathogenesis. Using a reverse genetic system for the SARS-CoV-2 WA1 isolate, we generated
226 a mutant virus that deleted the four amino acid insertion (Δ PRRA). The loss of the furin
227 cleavage site resulted in reduced infection in Calu3 respiratory cells and ablated disease in the
228 hamster pathogenesis model of SARS-CoV-2. Despite attenuated disease on initial infection,
229 the Δ PRRA infected hamsters were protected from subsequent challenge with WT SARS-CoV-2
230 indicating induction of robust immunity. Together, the results highlight the importance of the
231 furin cleavage site insertion to SARS-CoV-2 infection and pathogenesis.

232 Notably, despite attenuated disease *in vivo*, the Δ PRRA mutant had advantages over
233 WT SARS-CoV-2 and may complicate research studies. The Δ PRRA mutant has a fitness
234 advantage over the WT strain and dominated *in vitro* competition assays in Vero E6 compared
235 to WT virus. Importantly, the furin site deletion has been reported in SARS-CoV-2 preparations
236 ²² and given its fitness advantage in Vero E6 cells, can easily become the dominant tissue
237 culture adaption in virus preparations. Coupled with *in vitro* and *in vivo* attenuation, efforts must
238 be made to verify and evaluate stocks prior to critical studies. This also has implications for
239 manufacturing inactivated COVID19 vaccine on Vero cells ²³. Similarly, the shift in antibody
240 neutralization values of the Δ PRRA virus indicates the possibility of inaccurate results if this
241 mutation appears and distinguishes results from pseudotyped particles with and without this
242 furin mutations ²⁴. Fortunately, the Δ PRRA mutation will under represent the level of SARS-
243 CoV-2 neutralization rather than overstating protection level; however, with potential vaccine
244 and therapeutics decisions resting on these PRNT₅₀ values, accuracy must be paramount.
245 Together, the data highlight the importance of recognizing the mutation for future SARS-CoV-2
246 experimental analysis.

247 Biologically, the loss of the furin site shifts the processing of the spike in a cell type
248 dependent manner. In Vero E6 cells, ΔPRRA significantly reduces cleavage to the S1/S2 form
249 on the virion and the spike protein remains in the full-length conformation mirroring the results
250 observed for SARS-CoV. In contrast, WT SARS-CoV-2 processes nearly 60% of its spike to
251 S1/S2 indicating that most spike on the virion surface have been cleaved. Notably, the spike
252 processing is distinct in Calu3 2B4 respiratory cells. While SARS-CoV virions remain uncleaved
253 with little S1/S2 cleavage product, WT SARS-CoV-2 has increased processing from full-length
254 to the S1/S2 cleavage product than what was observed in Vero E6 cells. Surprisingly, ΔPRRA
255 in Calu3 cells also had a shift toward the S1/S2 fragment which is absent in Vero E6 cells. The
256 results indicate that while the majority of the spike cleavage in SARS-CoV-2 is mediated by the
257 furin cleavage site, there is more spike processing in SARS-CoV-2 even in its absence. With
258 known serine protease differences between Vero E6 and Calu3 2B4 cells ²⁵, the results suggest
259 that spike processing varies based on cell type and may contribute to altered infection and
260 pathogenesis *in vivo*.

261 In hamsters, the loss of the furin site attenuates SARS-CoV-2 induced disease, but does
262 not ablate ΔPRRA virus replication. Following challenge, hamsters infected with the ΔPRRA had
263 minimal change in weight loss over the first 10 DPI. In contrast, WT SARS-CoV-2 infected
264 hamsters lost ~15% of their body weight and showed signs of disease (hunching, diminished
265 movement, ruffled fur). While WT infected hamsters recovered, the absence of disease in the
266 ΔPRRA infected hamsters indicates a key role for the furin cleavage site in virulence.
267 Surprisingly, the ΔPRRA mutant was not attenuated in virus replication. At 3 and 4 DPI, the
268 ΔPRRA had augmented titers as compared to control in nasal washes and increased viral RNA
269 in the oral swabs. Similarly, the virus cleared one day later than WT SARS-CoV-2 during
270 primary challenge. The results suggest that the reduced disease observed following ΔPRRA
271 challenge was not a result of attenuated replication in these tissues.

272 Despite the lack of weight loss from initial challenge, ΔPRRA infected hamsters were
273 protected from further WT SARS-CoV-2 infection. After 28 days, ΔPRRA and WT infected
274 hamsters were rechallenged with WT SARS-CoV-2 and were protected from weight loss. While
275 mild disease was observed in one of the WT SARS-CoV-2 infected hamsters, the ΔPRRA
276 infected hamsters showed no evidence of disease. However, low viral loads were observed in
277 both the nasal washes and oral swabs from both groups, suggesting that the hamsters could
278 foster a low level of infection after rechallenge. Yet, the virus was rapidly cleared and failed to
279 induce disease in both groups, suggesting that adequate protection had been induced.
280 Together, the results suggest that ΔPRRA mutant, despite attenuated disease, induces
281 sufficient immunity to protect hamsters from further SARS-CoV-2 infection.

282 Overall, the data presented in this manuscript illustrate the critical role the furin cleavage
283 site insertion in the spike protein plays in SARS-CoV-2 infection and pathogenesis. In its
284 absence, the mutant ΔPRRA virus is attenuated in its ability to replicate in certain cell types and
285 to cause disease *in vivo*. However, the results are complicated by augmented replication and
286 fitness in Vero cells. Similarly, altered antibody neutralization profiles indicate a critical need to
287 survey this mutation in analysis of SARS-CoV-2 treatments and vaccines moving forward.
288 Together, the work highlights the critical nature of the furin cleavage site in understanding
289 SARS-CoV-2 infection and pathogenesis.

290

291 **Methods**

292 **Viruses and cells.** The recombinant wild-type and mutant SARS-CoV-2 are based on the
293 sequence of USA-WA1/2020 isolate provided by the World Reference Center for Emerging
294 Viruses and Arboviruses (WRCEVA) and was originally obtained from the USA Centers of
295 Disease Control as described ¹⁶. Wild-type and mutant SARS-CoV-2 as well as recombinant
296 mouse-adapted recombinant SARS-CoV ²⁶ were titrated and propagated on Vero E6 cells,
297 grown in DMEM with 5% fetal bovine serum and 1% antibiotic/antimyotic (Gibco). Calu3 2B4
298 cells were grown in DMEM with 10% defined fetal bovine serum, 1% sodium pyruvate (Gibco),
299 and 1% antibiotic/antimitotic (Gibco). Standard plaque assays were used for SARS-CoV and
300 SARS-CoV-2 ^{27,28}. All experiments involving infectious virus were conducted at the University of
301 Texas Medical Branch (Galveston, TX) or Emory University (Atlanta, Georgia) in approved
302 biosafety level 3 (BSL) laboratories with routine medical monitoring of staff.

303 **Construction of ΔPRRA Mutant Viruses.** Both wild-type and mutant viruses were derived
304 from the SARS-CoV-2 USA-WA1/2020 infectious clone as previously described ¹⁴. For ΔPRRA
305 mutant construction, the mutation was introduced into a subclone puc57-CoV2-F6 by using
306 overlap PCR with primers ΔPRRA-F (5'-GACTAATTCTCGTAGTGTAGCTAGTCAATCCATC-
307 3') and ΔPRRA-R (5'-GACTAGCTACACTACGAGAATTAGTCTGAGTC-3'). The resulted
308 plasmid was validated by restriction enzyme digestion and Sanger sequencing. Thereafter,
309 plasmids containing wild-type and mutant SARS-CoV-2 genome fragments were amplified and
310 restricted. The SARS-CoV-2 genome fragments were purified and ligated *in vitro* to assemble
311 the full-length cDNA according to the procedures described previously¹⁴. *In vitro* transcription
312 reactions were then preformed to synthesize full-length genomic RNA. To recover the viruses,
313 the RNA transcripts were electroporated into Vero E6 cells. The media from electroporated cells
314 were harvested at 40-hour post-infection and served as seed stocks for subsequent
315 experiments. Viral mutants were confirmed by sequence analysis prior to use. Synthetic

316 construction of SARS-CoV-2 ΔPRRA mutant was approved by the University of Texas Medical
317 Branch Institutional Biosafety Committee.

318 ***In Vitro Infection.*** Viral replication in Vero E6 and Calu3 2B4 cells were performed as
319 previously described ^{29,30}. Briefly, cells were washed with PBS and inoculated with SARS-CoV
320 or SARS-CoV-2 at a multiplicity of infection (MOI) 0.01 for 60 minutes at 37 °C. Following
321 inoculation, cells were washed, and fresh media was added to signify time 0. Three or more
322 biological replicates were harvested at each described time. No blinding was used in any
323 sample collections, nor were samples randomized.

324 ***Virion Purification and Western Blot.*** Vero E6 or Calu3-2B4 cells were infected with WT or
325 PRRA mutant viruses at an MOI of 0.01. At 24/48 HPI, the culture media were collected and
326 clarified by low speed spin. Virus particles in the media were subsequently pelleted by
327 ultracentrifugation through a 20% sucrose cushion at 26,000 rpm for 3 h by using a Beckman
328 SW28 rotor. For western blot analysis, protein lysates were prepared from the pellets using 2X
329 Laemmli Sample buffer (Cat# 161-073, BioRad, Hercules, Ca). Relative viral protein levels were
330 then determined by SDS-Page followed by western blot analysis as previously described ^{16,31}.
331 Briefly, sucrose purified SARS-CoV-1, SARS-CoV-2, and SARS-CoV-2 ΔPRRA inactivated by
332 boiling in Laemmeli Buffer. Samples were loaded in equal volumes into 4-20% Mini-PROTEAN
333 TGX Gels (Biorad# 4561093) and electrophoresed by SDS-Page. Protein was then transferred
334 to polyvinylidene difluoride (PVDF) membranes. Membranes were then blotted with SARS-CoV
335 Spike (S) specific antibodies (Novus Biologicals #NB100-56576), followed by probing with
336 horseradish peroxidase (HRP)-conjugated anti-rabbit antibody (Cell Signaling Technology
337 #7074S) as a secondary. Blots were then stripped and re-probed with SARS-CoV Nucleocapsid
338 (N) specific antibodies (provided as a kind gift from Dr. Shinji Makino) and the HRP-conjugated
339 anti-rabbit secondary. In both cases, signal was developed by treating membranes with Clarity

340 Western ECL substrate (Bio-Rad #1705060) imaging on a ChemiDoc MP System (Bio-Rad
341 #12003154). Densitometry was performed using ImageLab 6.0.1 (Bio-Rad #12012931).

342 **Competition Assay and Real-Time PCR.** For competition assays, ratios (50:50, 90:10, 10:90
343 WT/ ΔPRRA) were determined by plaque forming units derived from viral stocks. Vero cells
344 were infected at MOI 0.1 (WTn+ ΔPRRA) as described above. RNA from cell lysates were
345 collected using Trizol reagent (Invitrogen). RNA was then extracted from Triazol using the
346 Direct-zol RNA Miniprep Plus kit (Zymo Research #R2072) per the manufacturer's instruction.
347 Extracted RNA was then converted to cDNA with the iScript cDNA Synthesis kit (BioRad
348 #1708891). Quantitative real time PCR (qRT-PCR) was performed with the Luna Universal
349 qPCR Master Mix (New England Biolabs #M3003) on a CFX Connect instrument (BioRad
350 #1855200). For differentiation between wild type SARS-CoV-2 and SARS-CoV-2 ΔPRRA
351 genomes in competition experiments, Primer 1 (Forward - AAT GTT TTT CAA ACA CGT GCA
352 G and Primer 2 (Reverse - TAC ACT ACG TGC CCG CCG AGG) were used to detect wild type
353 genomes only. For detecting total genomes, Primer 1 and Primer 3 (Reverse - GAA TTT TCT
354 GCA CCA AGT GAC A) were used. 8-point standard curves (1x10¹ to 1x10⁸ copies/ μL) were
355 utilized to quantify the signal. A primer annealing temperature of 63°C was used for all assays.

356 For detection of viral RNA the nasal washes and oral swabs of SARS-CoV-2 and SARS-CoV-2
357 ΔPRRA infected hamsters, RNA extraction, cDNA synthesis, and qRT-PCR were performed as
358 described above. For qRT-PCR, Primer 1 and Primer 3 were utilized for all hamster samples.

359 **Deep Sequencing Analysis.** RNA libraries were prepared with 300ng of RNA using the Click-
360 Seq protocol as previously described ³² using tiled primers cognate to the SARS-CoV-2
361 genome (accession number NC_045512.2) and the TruSeq i7 LT adapter series and i5
362 hexamer adaptors containing a 12N unique molecular identifier (UMI). Libraries were
363 sequenced on the Illumina MiSeq platform with MiSeq Reagent Kit v2. Raw data was de-
364 multiplexed using TruSeq indexes using the MiSeq Reporter Software. Fastp v0.12. ³³ was used

365 to trim adapter sequences and low-quality reads ($q<25$), remove reads less than 40 nts in
366 length, and copy UMI sequences onto the read name. Reads were aligned with bowtie using the
367 -best parameter and allowing for up to two mismatches. The alignment index was generated
368 from a single fasta file, which contained two 600nt reference sequences spanning the PRRA
369 locus (23603-23616) of the wildtype (accession number NC_045512.2) and Δ PRRA genomes.
370 The alignments were sorted and indexed using Samtools v1.9³⁴, PCR duplicates were removed
371 using umi_tools³⁵. Coverage at each position was determined with the genomecov function in
372 bedtools v2.25.0³⁶.

373 **Plaque reduction neutralization titer assay.** Neutralization assays were preformed using
374 mNeonGreen SARS-CoV-2 reporter neutralization assay as previously described²¹. Briefly,
375 Vero E6 cells were plated black μ CLEAR flat-bottom 96-well plate (Greiner Bio-oneTM). On
376 following day, sera or monoclonal antibodies were serially diluted from 1/20 with nine 2-fold
377 dilutions to the final dilution of 1/5120 and incubated with mNeonGreen SARS-CoV-2 or Δ PRRA
378 expressing mNeonGreen at 37°C for 1 h. The virus-serum mixture was transferred to the Vero
379 E6 cell plate with the final multiplicity of infection (MOI) of 0.5. After 20 hours, Hoechst 33342
380 Solution (400-fold diluted in Hank's Balanced Salt Solution; Gibco) was added to stain cell
381 nucleus, sealed with Breath-Easy sealing membrane (Diversified Biotech), incubated at 37°C for
382 20 min, and quantified for mNeonGreen fluorescence on CytaionTM 7 (BioTek). The raw images
383 (2x2 montage) were acquired using 4x objective, processed, and stitched using the default
384 setting. The total cells (indicated by nucleus staining) and mNeonGreen-positive cells were
385 quantified for each well. Infection rates were determined by dividing the mNeonGreen-positive
386 cell number to total cell number. Relative infection rates were obtained by normalizing the
387 infection rates of serum-treated groups to those of non-serum-treated controls. The curves of
388 the relative infection rates versus the serum dilutions (\log_{10} values) were plotted using Prism 8
389 (GraphPad). A nonlinear regression method was used to determine the dilution fold that
390 neutralized 50% of mNeonGreen fluorescence (NT50). Each serum was tested in duplicates.

391 **Phylogenetic Tree, Sequence Identity Heat Map, and Structural modeling.** Heat maps were
392 constructed from a set of representative group 2B coronaviruses by using alignment data paired
393 with neighbor-joining phylogenetic trees built in Geneious (v.9.1.5) using the spike amino acid
394 sequences derived the following accession numbers: QHU79204 (SARS-CoV-2 WA1),
395 QHR63300.2 (RATG13), QND76034.1 (HKU3), AGZ48828.1 (WIV1), AGZ48806 (RsSHC014),
396 ALK02457 (WIV16), and AYV99817.1(SARS-CoV Urbani). Sequence identity was visualized
397 using EvolView (<http://evolgenius.info/>) and utilized SARS-CoV Co-V-2 WA1 as the reference
398 sequence. Tree shows the degree of genetic similarity of SARS-CoV-2 and SARS-CoV across
399 a selected group 2B coronaviruses. Structural models were generated using SWISS-Model ^{37,38}
400 to generate homology models for SARS-CoV-2 spike with and without the furin cleavage site
401 insertion based on the SARS-CoV-1 trimer structure (PDB 6ACD). Homology models were
402 visualized and manipulated in MacPyMol (version 1.3).

403 **Animals and ethics statements.** Male Syrian hamsters (7-8 weeks old, 86–127□g) were
404 purchased from Envigo. All procedures were conducted under an animal protocol approved by
405 the UTMB Institutional Animal Care and Use Committee and complied with USDA guidelines in
406 an AAALAC-accredited lab. Work with infectious SARS-CoV-2 in hamsters was performed in
407 the Galveston National Laboratory BSL-4 laboratory. Animals were housed in microisolator
408 caging equipped with HEPA filters in the BSL-4 laboratories.

409 **Hamster Infection studies.** Hamsters were challenged with 10^5 PFU of WT-SARS-CoV-2 or
410 SARS-CoV-2 Δ PRRA by intranasal inoculation (i.n.). Hamsters were observed daily for the
411 development of clinical disease and body weights were taken every day for the first 10 days of
412 the study, then every third day. For each manipulation (viral infection, retro-orbital bleeds, nasal
413 wash, or oral swab), animals were anesthetized with isoflurane (Piramal, Bethlehem, PA).

414 **Statistical analysis.** All statistical comparisons in this manuscript involved the comparison
415 between 2 groups, SARS-CoV or SARS-CoV-2 infected groups under equivalent conditions.

416 Thus, significant differences in viral titer were determined by the unpaired two-tailed students T-
417 Test.

418 **Data Availability.** The raw data that support the findings of this study are available from the
419 corresponding author upon reasonable request.

420 **Acknowledgements.** Research was supported by grants from NIA and NIAID of the NIH to
421 (AI153602 and AG049042 to VDM AI142759, AI134907, AI145617, and UL1TR001439 to P-
422 YS; R01AI123449 to AF and BL; R24AI120942 (WRCEVA) to SCW). Research was also
423 supported by STARS Award provided by the University of Texas System to VDM and trainee
424 funding provided by the McLaughlin Fellowship Fund at UTMB. P-YS was also supported by
425 CDC grant for the Western Gulf Center of Excellence for Vector-Borne Diseases, and awards
426 from the Sealy & Smith Foundation, Kleberg Foundation, John S. Dunn Foundation, Amon G.
427 Carter Foundation, Gilson Longenbaugh Foundation, and Summerfield Robert Foundation.

428 **Author Contributions**

429 Conceptualization, XX, BAJ, ALR, MS, ANF, P-YS, and VDM; Methodology, BAJ, XX, BK, KGL,
430 DS, ALR, ANF, P-YS and VDM.; Investigation, BAJ, XX, BK, KGL, AM, JZ, XZ, TJ, JKS, LZ, CS,
431 MV, AV, DS, NB, JAP, ALR, KD, and VDM.; Resources, KSP, SCW, MSS, PR, ZK, ZA, P-YS,
432 ANF, VDM; Data Curation, BAJ, XX, BK, KGL, AV, DS, ALR, MSS, KD, P-YS, ANF, VDM.;
433 Writing-Original Draft, VDM; Writing-Review & Editing, BAJ, XX, BL, PA, MSS, KD, ZK, ZA, P-
434 YS, ANF, VDM.; Visualization, XX, BAJ, BK, KGL, NB, ANF, VDM; Supervision, PA, SCW,
435 MSS, P-YS, ANF, VDM.; Funding Acquisition, PA, SCW, PY-S, ANF, VDM.

436 **Competing interests**

437 X.X., V.D.M., and P.-Y.S. have filed a patent on the reverse genetic system and reporter SARS-
438 CoV-2. Other authors declare no competing interests.

439

440 **References**

- 441 1. Gralinski, L.E. & Menachery, V.D. Return of the Coronavirus: 2019-nCoV. *Viruses*
442 **12**(2020).
- 443 2. Dong, E., Du, H. & Gardner, L. An interactive web-based dashboard to track COVID-19
444 in real time. *Lancet Infect Dis* **20**, 533-534 (2020).
- 445 3. Zhu, N., et al. A Novel Coronavirus from Patients with Pneumonia in China, 2019. *N
446 Engl J Med* **382**, 727-733 (2020).
- 447 4. Huang, C., et al. Clinical features of patients infected with 2019 novel coronavirus in
448 Wuhan, China. *Lancet* **395**, 497-506 (2020).
- 449 5. Gao, Z., et al. A Systematic Review of Asymptomatic Infections with COVID-19. *J
450 Microbiol Immunol Infect* (2020).
- 451 6. Shang, J., et al. Structural basis of receptor recognition by SARS-CoV-2. *Nature* **581**,
452 221-224 (2020).
- 453 7. Yuan, M., et al. A highly conserved cryptic epitope in the receptor binding domains of
454 SARS-CoV-2 and SARS-CoV. *Science* **368**, 630-633 (2020).
- 455 8. Lu, G., Wang, Q. & Gao, G.F. Bat-to-human: spike features determining 'host jump' of
456 coronaviruses SARS-CoV, MERS-CoV, and beyond. *Trends in microbiology* **23**, 468-478
457 (2015).
- 458 9. Coutard, B., et al. The spike glycoprotein of the new coronavirus 2019-nCoV contains a
459 furin-like cleavage site absent in CoV of the same clade. *Antiviral Res* **176**, 104742 (2020).
- 460 10. Seidah, N.G. & Chretien, M. Proprotein and prohormone convertases: a family of
461 subtilases generating diverse bioactive polypeptides. *Brain Res* **848**, 45-62 (1999).
- 462 11. Braun, E. & Sauter, D. Furin-mediated protein processing in infectious diseases and
463 cancer. *Clin Transl Immunology* **8**, e1073 (2019).
- 464 12. de Haan, C.A., et al. Cleavage of group 1 coronavirus spike proteins: how furin cleavage
465 is traded off against heparan sulfate binding upon cell culture adaptation. *Journal of virology* **82**,
466 6078-6083 (2008).
- 467 13. Kirchdoerfer, R.N., et al. Pre-fusion structure of a human coronavirus spike protein.
468 *Nature* **531**, 118-121 (2016).
- 469 14. Xie, X., et al. An Infectious cDNA Clone of SARS-CoV-2. *Cell host & microbe* **27**, 841-
470 848 e843 (2020).
- 471 15. Song, W., Gui, M., Wang, X. & Xiang, Y. Cryo-EM structure of the SARS coronavirus
472 spike glycoprotein in complex with its host cell receptor ACE2. *PLoS pathogens* **14**, e1007236
473 (2018).
- 474 16. Harcourt, J., et al. Severe Acute Respiratory Syndrome Coronavirus 2 from Patient with
475 2019 Novel Coronavirus Disease, United States. *Emerg Infect Dis* **26**(2020).
- 476 17. Sims, A.C., et al. Release of severe acute respiratory syndrome coronavirus nuclear
477 import block enhances host transcription in human lung cells. *Journal of virology* **87**, 3885-3902
478 (2013).
- 479 18. Menachery, V.D., et al. Pathogenic Influenza A viruses and SARS-CoV viruses
480 modulate global interferon stimulated gene induction through diverse mechanisms. *Cytokine* **59**,
481 556-556 (2012).
- 482 19. Zhou, P., et al. A pneumonia outbreak associated with a new coronavirus of probable
483 bat origin. *Nature* **579**, 270-273 (2020).
- 484 20. Imai, M., et al. Syrian hamsters as a small animal model for SARS-CoV-2 infection and
485 countermeasure development. *Proceedings of the National Academy of Sciences of the United
486 States of America* **117**, 16587-16595 (2020).
- 487 21. Muruato, A.E., et al. A high-throughput neutralizing antibody assay for COVID-19
488 diagnosis and vaccine evaluation. *Nature communications* **11**, 4059 (2020).

489 22. Davidson, A.D., et al. Characterisation of the transcriptome and proteome of SARS-CoV-
490 2 reveals a cell passage induced in-frame deletion of the furin-like cleavage site from the spike
491 glycoprotein. *Genome Med* **12**, 68 (2020).

492 23. Gao, Q., et al. Development of an inactivated vaccine candidate for SARS-CoV-2.
493 *Science* **369**, 77-81 (2020).

494 24. Hansen, J., et al. Studies in humanized mice and convalescent humans yield a SARS-
495 CoV-2 antibody cocktail. *Science* (2020).

496 25. Abe, M., et al. TMPRSS2 is an activating protease for respiratory parainfluenza viruses.
497 *Journal of virology* **87**, 11930-11935 (2013).

498 26. Roberts, A., et al. A mouse-adapted SARS-coronavirus causes disease and mortality in
499 BALB/c mice. *PLoS pathogens* **3**, e5 (2007).

500 27. Sims, A.C., et al. Release of severe acute respiratory syndrome coronavirus nuclear
501 import block enhances host transcription in human lung cells. *J Virol* **87**, 3885-3902 (2013).

502 28. Josset, L., et al. Cell host response to infection with novel human coronavirus EMC
503 predicts potential antivirals and important differences with SARS coronavirus. *MBio* **4**, e00165-
504 00113 (2013).

505 29. Sheahan, T., Rockx, B., Donaldson, E., Corti, D. & Baric, R. Pathways of cross-species
506 transmission of synthetically reconstructed zoonotic severe acute respiratory syndrome
507 coronavirus. *Journal of virology* **82**, 8721-8732 (2008).

508 30. Menachery, V.D., et al. Attenuation and restoration of severe acute respiratory syndrome
509 coronavirus mutant lacking 2'-o-methyltransferase activity. *Journal of virology* **88**, 4251-4264
510 (2014).

511 31. van Tol, S., et al. VAMP8 Contributes to the TRIM6-Mediated Type I Interferon Antiviral
512 Response during West Nile Virus Infection. *Journal of virology* **94** (2020).

513 32. Routh, A., Head, S.R., Ordoukhanian, P. & Johnson, J.E. ClickSeq: Fragmentation-Free
514 Next-Generation Sequencing via Click Ligation of Adaptors to Stochastically Terminated 3'-
515 Azido cDNAs. *J Mol Biol* **427**, 2610-2616 (2015).

516 33. Chen, S., Zhou, Y., Chen, Y. & Gu, J. fastp: an ultra-fast all-in-one FASTQ preprocessor.
517 *Bioinformatics* **34**, i884-i890 (2018).

518 34. Li, H., et al. The Sequence Alignment/Map format and SAMtools. *Bioinformatics* **25**,
519 2078-2079 (2009).

520 35. Smith, T., Heger, A. & Sudbery, I. UMI-tools: modeling sequencing errors in Unique
521 Molecular Identifiers to improve quantification accuracy. *Genome Res* **27**, 491-499 (2017).

522 36. Quinlan, A.R. & Hall, I.M. BEDTools: a flexible suite of utilities for comparing genomic
523 features. *Bioinformatics* **26**, 841-842 (2010).

524 37. Waterhouse, A., et al. SWISS-MODEL: homology modelling of protein structures and
525 complexes. *Nucleic Acids Res* **46**, W296-W303 (2018).

526 38. Bienert, S., et al. The SWISS-MODEL Repository-new features and functionality. *Nucleic
527 Acids Res* **45**, D313-D319 (2017).

528

529

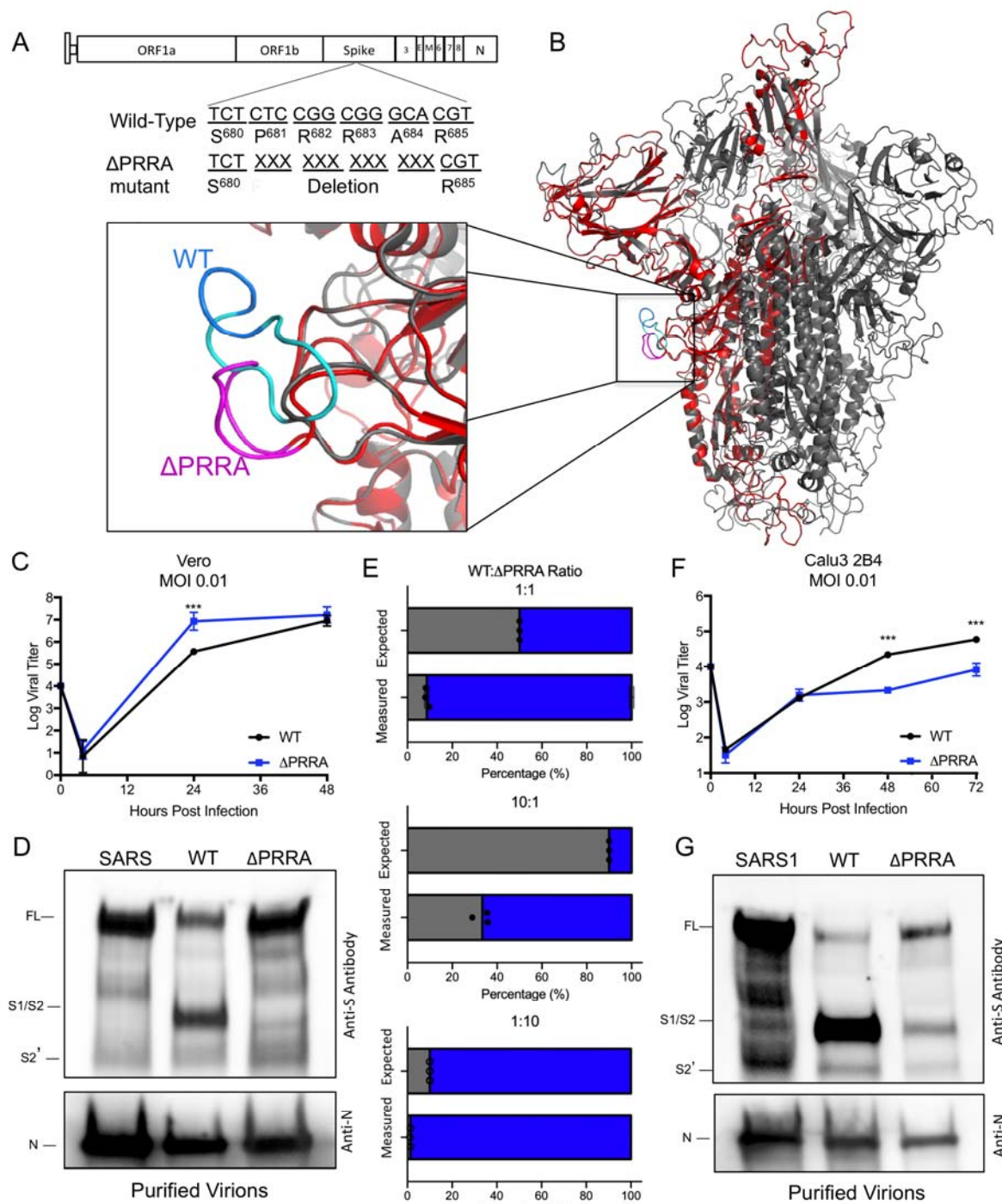
530 **Figure Legends**

531 **Figure 1. Distinct replication, spike cleavage, and competition for ΔPRRA.** A) Generation
532 of a SARS-CoV-2 mutant deleting the furin cleavage site insertion from the spike protein. B)
533 Structure of the SARS-CoV-2 spike trimer with a focus on the furin cleavage site (inset).
534 Modeled using the SARS-CoV-1 trimer structure (PDB 6ACD) (14), the WT SARS-CoV-2 trimer
535 (grey) with SARS-CoV-2 PRRA deletion mutant monomer overlay (red). The loop (inset), which
536 is unresolved on SARS-CoV-2 structures (AA 691-702), is shown in cyan on SARS-CoV-2 with
537 the PRRA sequence in blue. The loop region in the PRRA deletion mutant is shown in pink.
538 C) Viral titer from Vero E6 cells infected with WT SARS-CoV-2 (black) or ΔPRRA (blue) at MOI
539 0.01 (N=3). D) Purified SARS-CoV, SARS-CoV-2 WT, and ΔPRRA virions were probed with
540 anti-spike or anti-nucleocapsid antibody. Full length (FL), S1/S2 cleavage form, and S2'
541 annotated. E) Competition assay between SARS-CoV-2 WT (black) and ΔPRRA (blue) showing
542 RNA percentage based on quantitative RT-PCR at 50:50, 90:10, 10:90, 99:1, and 1:99 WT/
543 ΔPRRA ratio (N=3 per group). F) Viral titer from Calu3 2B4 cells infected with WT SARS-CoV-2
544 (black) or ΔPRRA (blue) at MOI 0.01 (N=3). G) Purified SARS-CoV, SARS-CoV-2 WT, and
545 ΔPRRA virions were probed with anti-spike or anti-nucleocapsid antibody. Full length (FL),
546 S1/S2 cleavage form, and S2' annotated. P-values based on Student T-test and are marked as
547 indicated: * <0.05 *** <0.001 .

548 **Figure 2. *In vivo* attenuation of ΔPRRA mutant.** A) Primary SARS-CoV-2 challenge
549 schematic. Two groups of male hamsters (N=4) were challenged with 10^5 plaque forming units
550 of either SARS-CoV-2 WT or ΔPRRA mutant and evaluated over a 28 day time course for B)
551 weight loss, C) disease score, D) viral titer from nasal wash, and E) viral RNA from oral swabs.
552 F) Schematic for rechallenge of previously infected hamsters. Twenty eight DPI, hamsters from
553 SARS-CoV-2 WT and ΔPRRA were rechallenged with 10^5 PFU of SARS-CoV-2 WT and
554 evaluated for G) weight loss, H) disease score, I) viral titer from nasal wash, and E) viral RNA

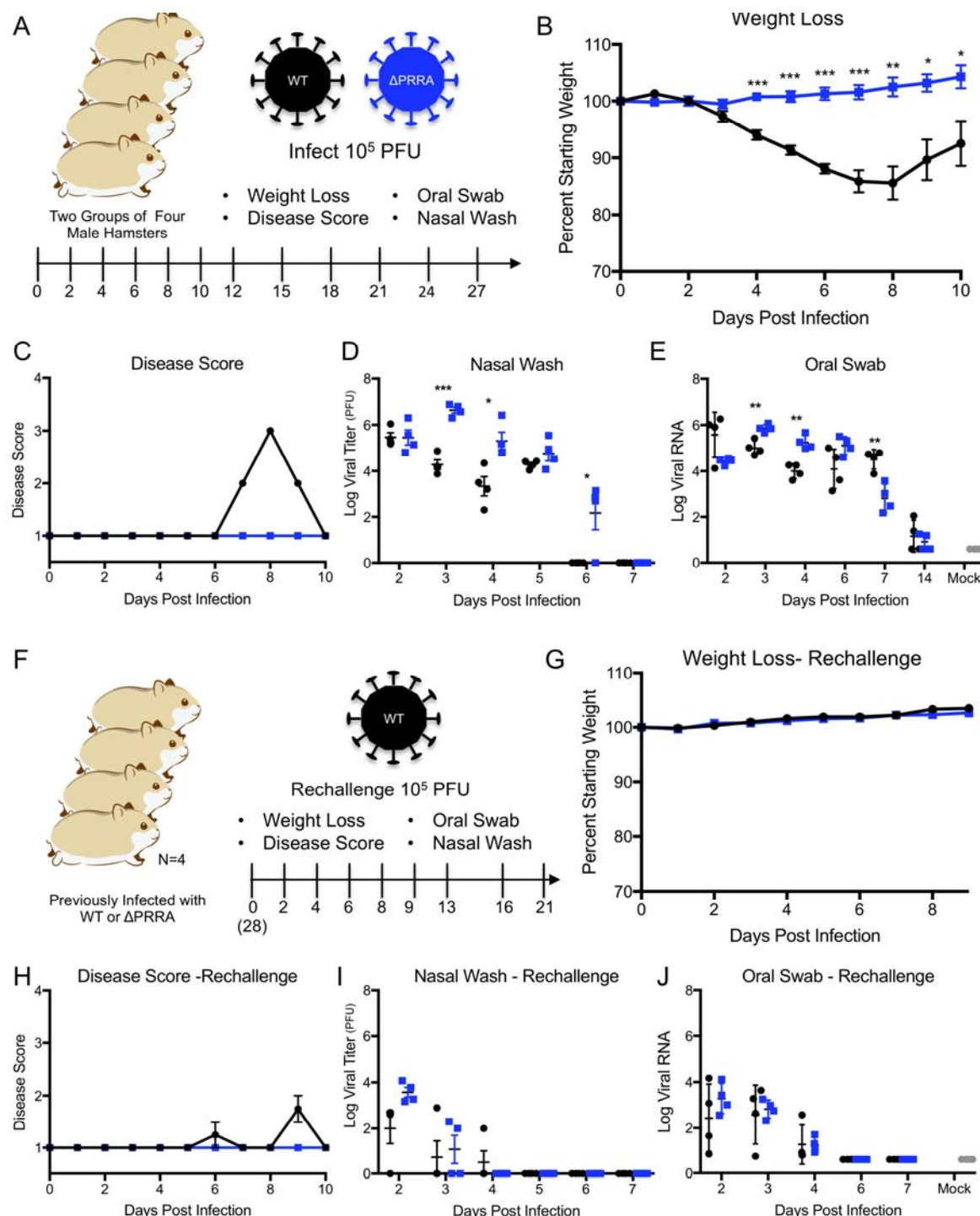
555 from oral swabs. P-values based on Student T-test and are marked as indicated: * <0.05
556 ** <0.01 *** <0.001 .

557 **Figure 3. Antibody neutralization of Δ PRRA mutant.** A) Schematic for SARS-CoV-2 Δ PRRA
558 reporter virus expressing mNeonGreen (mNG) gene in place of ORF7 equivalent to previously
559 described WT SARS-CoV-2 mNG virus²¹. B) Plaque reduction neutralization (PRNT₅₀) values
560 as measured by changes to mNG expression. PRNT₅₀ values plotted as Log (1/serum dilution)
561 with Δ PRRA on Y axis and WT-SARS-CoV-2. C-E) Representative curves from C) low, D)
562 intermediate, and E) high neutralizing COVID-19 patient sera. F-H) Neutralization curves from
563 mAB-1 (F), mAB-2 (G), and mAB-3 (H), N=3.



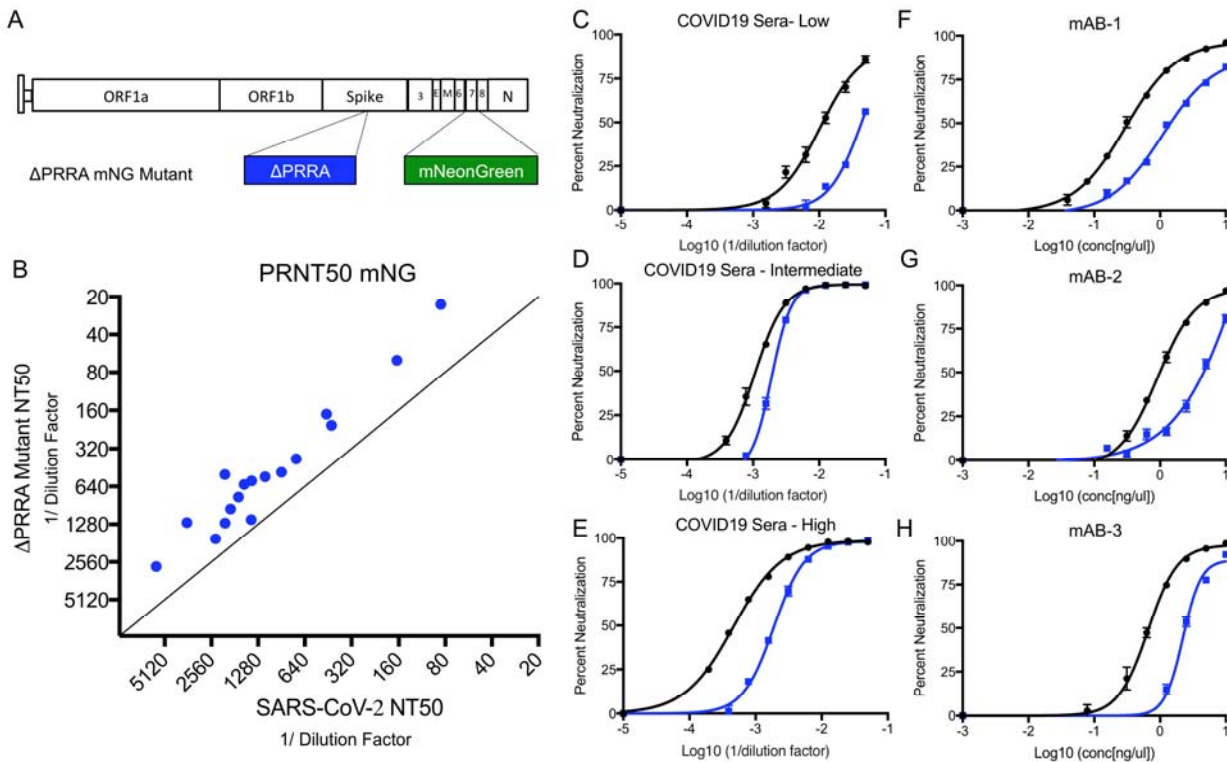
564
565 **Figure 1. Distinct replication, spike cleavage, and competition for ΔPRRA.** A) Generation
566 of a SARS-CoV-2 mutant deleting the furin cleavage site insertion from the spike protein. B)
567 Structure of the SARS-CoV-2 spike trimer with a focus on the furin cleavage site (inset).
568 Modeled using the SARS-CoV-1 trimer structure (PDB 6ACD) (14), the WT SARS-CoV-2 trimer
569 (grey) with SARS-CoV-2 PRRA deletion mutant monomer overlay (red). The loop (inset), which
570 is unresolved on SARS-CoV-2 structures (AA 691-702), is shown in cyan on SARS-CoV-2 with
571 the PRRA sequence in blue. The loop region in the PRRA deletion mutant is shown in pink.
572 C) Viral titer from Vero E6 cells infected with WT SARS-CoV-2 (black) or ΔPRRA (blue) at MOI
573 0.01 (N=3). D) Purified SARS-CoV, SARS-CoV-2 WT, and ΔPRRA virions were probed with

574 anti-spike or anti-nucleocapsid antibody. Full length (FL), S1/S2 cleavage form, and S2'
575 annotated. E) Competition assay between SARS-CoV-2 WT (black) and Δ PRRA (blue) showing
576 RNA percentage based on quantitative RT-PCR at 50:50, 90:10, 10:90, 99:1, and 1:99 WT/
577 Δ PRRA ratio (N=3 per group). F) Viral titer from Calu3 2B4 cells infected with WT SARS-CoV-2
578 (black) or Δ PRRA (blue) at MOI 0.01 (N=3). G) Purified SARS-CoV, SARS-CoV-2 WT, and
579 Δ PRRA virions were probed with anti-spike or anti-nucleocapsid antibody. Full length (FL),
580 S1/S2 cleavage form, and S2' annotated. P-values based on Student T-test and are marked as
581 indicated: * <0.05 *** <0.001 .
582



583
584
585
586
587
588
589
590
591

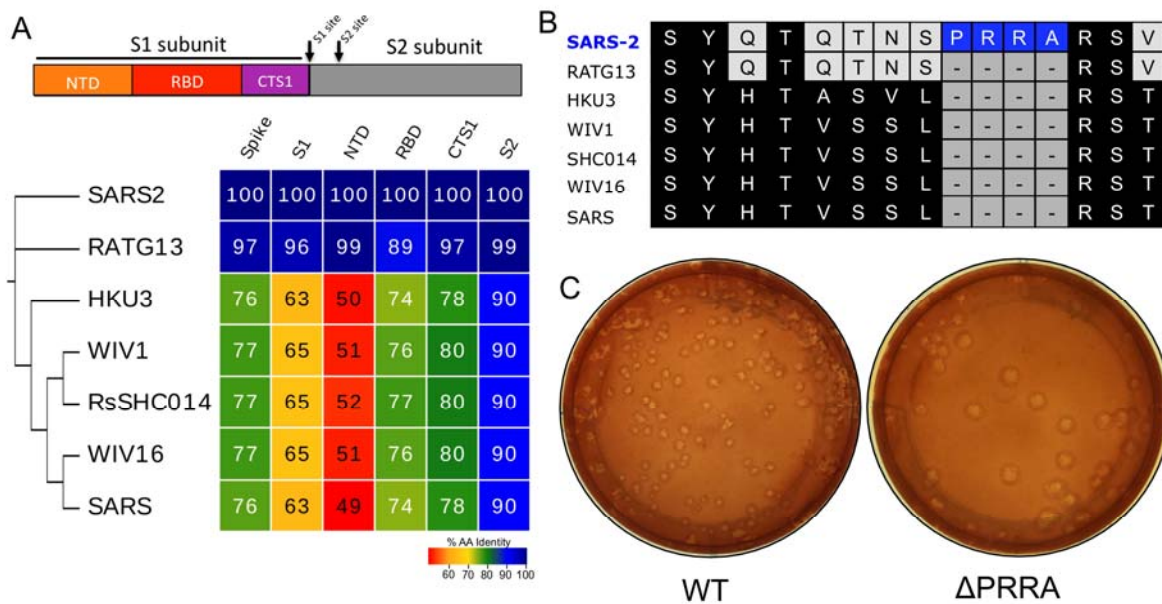
Figure 2. In vivo attenuation of ΔPRRA mutant. A) Primary SARS-CoV-2 challenge schematic. Two groups of male hamsters (N=4) were challenged with 10^5 plaque forming units of either SARS-CoV-2 WT or ΔPRRA mutant and evaluated over a 28 day time course for B) weight loss, C) disease score, D) viral titer from nasal wash, and E) viral RNA from oral swabs. F) Schematic for rechallenge of previously infected hamsters. Twenty eight DPI, hamsters from SARS-CoV-2 WT and ΔPRRA were rechallenged with 10^5 PFU of SARS-CoV-2 WT and evaluated for G) weight loss, H) disease score, I) viral titer from nasal wash, and E) viral RNA from oral swabs. P-values based on Student T-test and are marked as indicated: * <0.05 ** <0.01 *** <0.001 .



592

593 **Figure 3. Antibody neutralization of ΔPRRA mutant.** A) Schematic for SARS-CoV-2 ΔPRRA reporter
594 virus expressing mNeonGreen (mNG) gene in place of ORF7 equivalent to previously described WT
595 SARS-CoV-2 mNG virus¹⁴. B) Plaque reduction neutralization (PRNT₅₀) values as measured by changes
596 to mNG expression. PRNT₅₀ values plotted as Log (1/serum dilution) with ΔPRRA on Y axis and WT-
597 SARS-CoV-2 on the X axis. C-E) Representative curves from C) low, D) intermediate, and E) high
598 neutralizing COVID-19 patient sera. F-H) Neutralization curves from mAB-1 (F), mAB-2 (G), and mAB-3
599 (H), N=3.

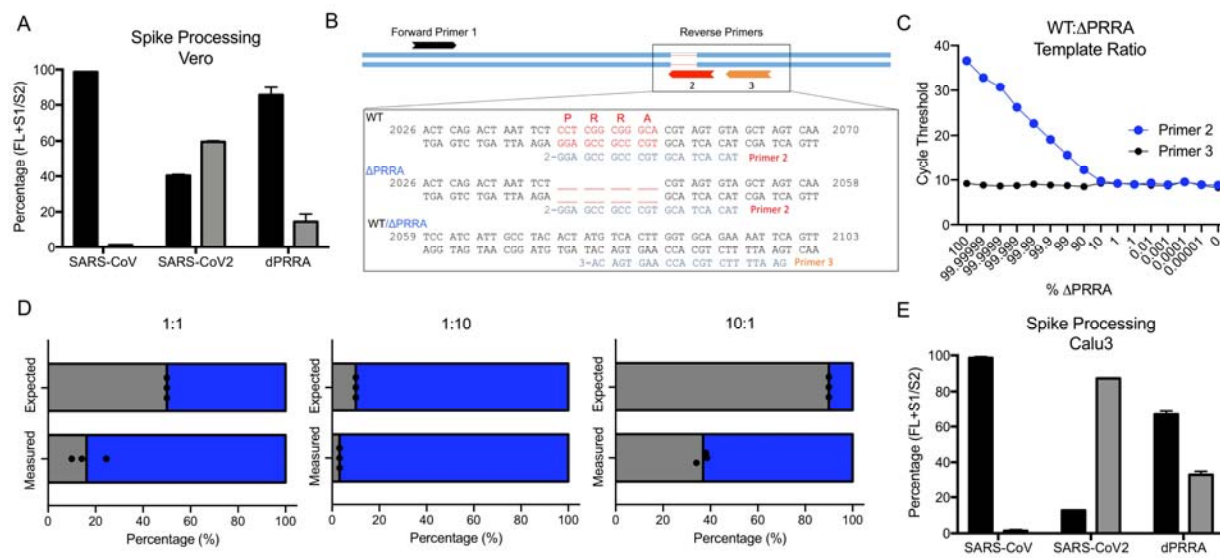
600

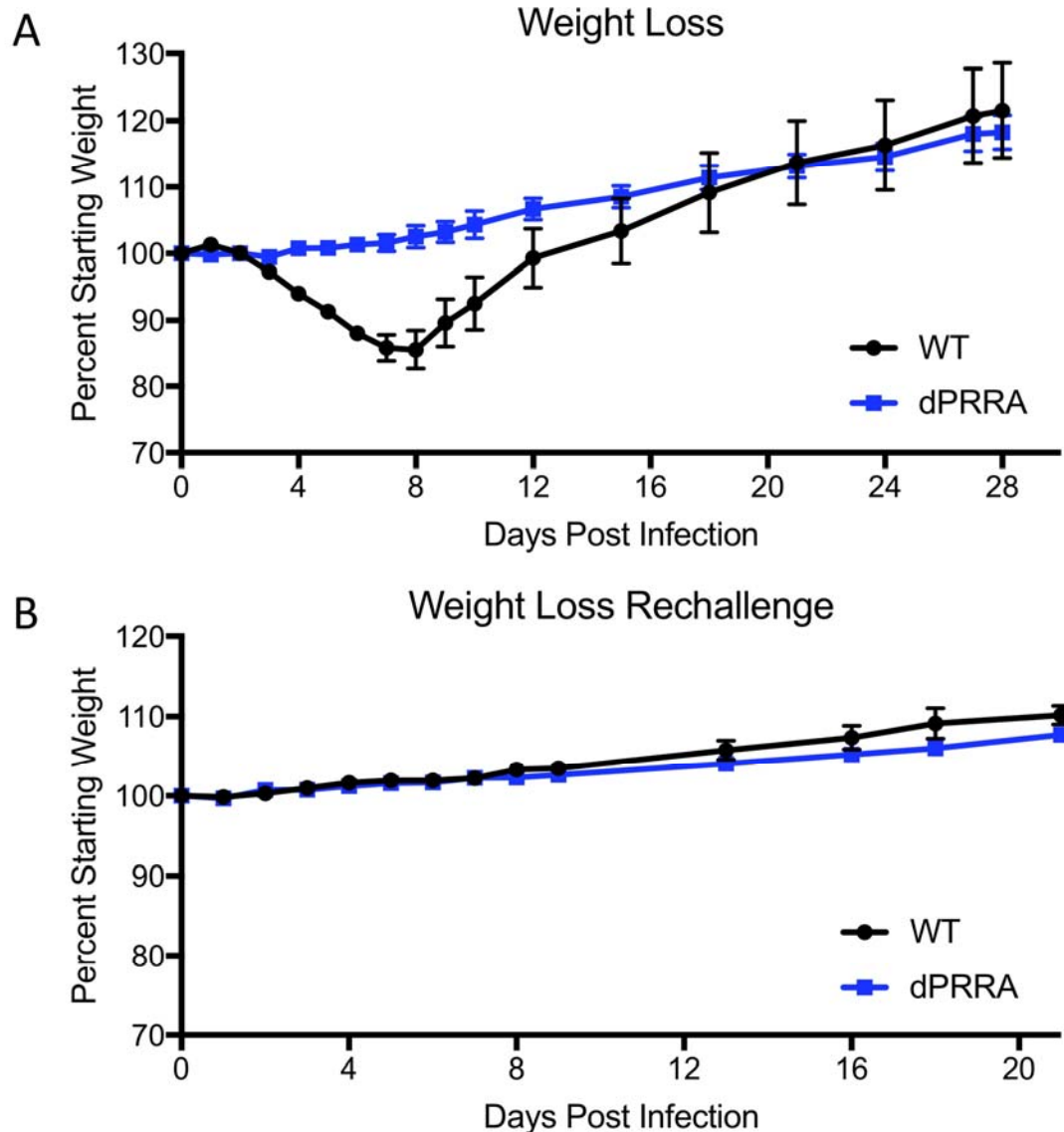


601

602 **S. Figure 1. Furin cleavage site in SARS-CoV-2 spike.** A) Diagram of the coronavirus spike protein
603 domains and cleavage sites. The sequences of the indicated group 2B coronaviruses were aligned
604 according to the bounds of total spike, S1, N-terminal domain (NTD), Receptor binding domain (RBD),
605 and C-terminal of S1 (CTS1) and S2. Sequence identities were extracted from the alignments, and a
606 heatmap of sequence identity was constructed using EvolView (www.evolgenius.info/evolview) with
607 SARS-CoV-2 WA1 as the reference sequence. B) Alignment of the furin cleavage site of SARS-CoV-2
608 and the corresponding amino acids identities found closely related group 2B CoVs. The PRRA insertion
609 is unique to SARS-CoV-2. C) Representative plaque morphology of WT and ΔPRRA SARS-CoV-2.

610





620

621 **S. Figure 3. *In vivo* attenuation of Δ PRRA mutant.** A) Weight loss following primary WT and Δ PRRA
622 mutant SARS-CoV-2 challenge (N=4 per group). B) Weight loss following rechallenge of WT and Δ PRRA
623 mutant infected mice with WT SARS-CoV-2 (N=4 per group).

624